

Polarization mode coupling and related effects in fiber Bragg grating inscribed in polarization maintaining fiber

Yanshuang Zhao,¹ Bo Sun,¹ Yanlei Liu,¹ Jing Ren,¹ Jianzhong Zhang,^{1,4} Jun Yang,^{1,5}
John Canning,^{2,3} G. D. Peng,² and Libo Yuan¹

¹*Key Lab of In-Fiber Integrated Optics of Ministry of Education, Harbin Engineering University, Harbin 150001, China*

²*Photonics & Optical Communications, School of Electrical Engineering & Telecommunications, University of New South Wales, Sydney 2052, NSW, Australia*

³*interdisciplinary Photonics Laboratories, School of Chemistry, The University of Sydney, NSW, 2006 Australia*

⁴zhangjianzhong@hrbeu.edu.cn

⁵yangjun@hrbeu.edu.cn

Abstract: Polarization mode coupling (PMC) and related effects from writing fiber Bragg gratings in polarization maintaining fiber (FBGs-in-PMF) are observed experimentally for the first time by optical fiber coherence domain polarimetry (OCDP) using a broadband light source. PMC is another useful aspect of FBG-in-PMF besides Bragg wavelength and its possible potential is evaluated and discussed. A localized and long range temperature measurement based on the PMC and Bragg wavelength is given as an example.

©2016 Optical Society of America

OCIS codes: (060.2420) Fibers, polarization-maintaining; (260.5430) Polarization; (060.3735) Fiber Bragg gratings; (060.2370) Fiber optics sensors.

References and links

1. C. M. Lawrence, D. V. Nelson, E. Udd, and T. Bennett, "A fiber optic sensor for transverse strain measurement," *Exp. Mech.* **39**(3), 202–209 (1999).
2. C. C. Ye, S. E. Staines, S. W. James, and R. P. Tatam, "A polarization-maintaining fiber Bragg grating interrogation system for multi-axis strain sensing," *Meas. Sci. Technol.* **13**(9), 1446–1449 (2002).
3. G. H. Chen, L. Y. Liu, H. Z. Jia, J. M. Yu, L. Xu, and W. C. Wang, "Simultaneous strain and temperature measurements with fiber Bragg grating written in novel Hi-Bi optical fiber," *IEEE Photonics Technol. Lett.* **16**(1), 221–223 (2004).
4. J. F. Botero-Cadavid, J. D. Causado-Buelvas, and P. Torres, "Spectral properties of locally pressed fiber Bragg gratings written in polarization maintaining fibers," *J. Lightwave Technol.* **28**(9), 1291–1297 (2010).
5. C. L. Zhao, X. F. Yang, C. Lu, N. J. Hong, X. Guo, P. R. Chaudhuri, and X. Y. Dong, "Switchable multi-wavelength erbium-doped fiber lasers by using cascaded fiber Bragg gratings written in high birefringence fiber," *Opt. Commun.* **230**(4–6), 313–317 (2004).
6. Y. Liu, X. Feng, S. Yuan, G. Kai, and X. Dong, "Simultaneous four-wavelength lasing oscillations in an erbium-doped fiber laser with two high birefringence fiber Bragg gratings," *Opt. Express* **12**(10), 2056–2061 (2004).
7. C. Spiegelberg, J. H. Geng, Y. D. Hu, Y. Kaneda, S. B. Jiang, and N. Peyghambarian, "Low-noise narrow-linewidth fiber laser at 1550 nm," *J. Lightwave Technol.* **22**(1), 57–62 (2004).
8. D. Inniss, Q. Zhong, A. M. Vengsarkar, W. A. Reed, S. G. Kosinski, and P. J. Lemaire, "Atomic force microscopy study of uv-induced anisotropy in hydrogen-loaded germanosilicate fibers," *Appl. Phys. Lett.* **65**(12), 1528–1530 (1994).
9. T. Erdogan and V. Mizrahi, "Characterization of UV-induced birefringence in photosensitive Ge-doped silica optical fibers," *J. Opt. Soc. Am. B* **11**(10), 2100–2105 (1994).
10. A. M. Vengsarkar, Q. Zhong, D. Inniss, W. A. Reed, P. J. Lemaire, and S. G. Kosinski, "Birefringence reduction in side-written photoinduced fiber devices by a dual-exposure method," *Opt. Lett.* **19**(16), 1260–1262 (1994).
11. J. Canning, M. Janos, and M. G. Sceats, "Rayleigh longitudinal profiling of optical resonances within waveguide grating structures using sidescattered light," *Opt. Lett.* **21**(8), 609–611 (1996).
12. K. Dossou, S. LaRochelle, and M. Fontaine, "Numerical Analysis of the Contribution of the transverse asymmetry in the photo-induced index change profile to the birefringence of optical fiber," *J. Lightwave Technol.* **20**(8), 1463–1470 (2002).
13. N. Belhadj, S. Larochelle, and K. Dossou, "Form birefringence in UV-exposed photosensitive fibers computed using a higher order finite element method," *Opt. Express* **12**(8), 1720–1726 (2004).

14. P. S. Russell and D. P. Hand, "Rocking filter formation in photosensitive high birefringence optical fibers," *Electron. Lett.* **26**(22), 1846–1848 (1990).
15. K. O. Hill, F. Bilodeau, B. Malo, and D. C. Johnson, "Birefringent photosensitivity in monomode optical fiber: application to external writing of rocking filters," *Electron. Lett.* **27**(17), 1548–1550 (1991).
16. K. S. Lee and J. Y. Cho, "Polarization-mode coupling in birefringent fiber gratings," *J. Opt. Soc. Am. A* **19**(8), 1621–1631 (2002).
17. G. Statkiewicz-Barabach, A. Anuszkiewicz, W. Urbanczyk, and J. Wojcik, "Sensing characteristics of rocking filter fabricated in microstructured birefringent fiber using fusion arc splicer," *Opt. Express* **16**(22), 17258–17268 (2008).
18. J. P. Carvalho, A. Anuszkiewicz, G. Statkiewicz-Barabach, J. M. Baptista, O. Frazão, P. Mergo, J. L. Santos, and W. Urbanczyk, "Long period gratings and rocking filters written with a CO₂ laser in highly-birefringent boron-doped photonic crystal fibers for sensing applications," *Opt. Commun.* **285**(3), 264–268 (2012).
19. G. Statkiewicz-Barabach, J. Olszewski, P. Mergo, and W. Urbanczyk, "Higher-order rocking filters induced mechanically in fibers with different birefringence dispersion," *Appl. Opt.* **53**(7), 1258–1267 (2014).
20. M. S. Müller, H. J. El-Khozondar, T. C. Buck, and A. W. Koch, "Analytical solution of four-mode coupling in shear strain loaded fiber Bragg grating sensors," *Opt. Lett.* **34**(17), 2622–2624 (2009).
21. F. Yang, Z. Fang, Z. Pan, Q. Ye, H. Cai, and R. Qu, "Orthogonal polarization mode coupling for pure twisted polarization maintaining fiber Bragg gratings," *Opt. Express* **20**(27), 28839–28845 (2012).
22. K. Takada, J. Noda, and K. Okamoto, "Measurement of spatial distribution of mode coupling in birefringent polarization-maintaining fiber with new detection scheme," *Opt. Lett.* **11**(10), 680–682 (1986).
23. S. Chen, I. P. Giles, and M. Fahadroushan, "Quasi-distributed pressure sensor using intensity-type optical coherence domain polarimetry," *Opt. Lett.* **16**(5), 342–344 (1991).
24. Z. Ding, Z. Meng, X. S. Yao, X. Chen, T. Liu, and M. Qin, "Accurate method for measuring the thermal coefficient of group birefringence of polarization-maintaining fibers," *Opt. Lett.* **36**(11), 2173–2175 (2011).
25. J. Yang, Y. Yuan, A. Zhou, J. Cai, C. Li, D. Yan, S. Huang, F. Peng, B. Wu, Y. Zhang, Z. Liu, and L. Yuan, "Full evaluation of polarization characteristics of multifunctional integrated optic chip with high accuracy," *J. Lightwave Technol.* **32**(22), 3641–3650 (2014).
26. M. A. Davis and A. D. Kersey, "Application of a fiber fourier transform spectrometer to the detection of wavelength-encoded signals from Bragg grating sensors," *J. Lightwave Technol.* **13**(7), 1289–1295 (1995).

1. Introduction

Fiber Bragg gratings inscribed in polarization maintaining fiber (FBGs-in-PMF) have been demonstrated around twenty years and applied in optical fiber sensors [1–4] and multi-wavelength or single polarized lasers [5–7]. Many of these applications utilize the different Bragg responses of the two polarization eigenstates introduced by the birefringence. This change can affect the birefringence given the stress response of the profile is along one axis - therefore the change across the core whilst uniform in real index is not uniform in the stress-optic response. The orientation of the writing beam becomes important, as does the polarization of the writing beam. Polarization mode coupling (PMC) between the eigenstates is weakest when the UV-induced index change is across the entire core or aligned orthogonal to the stress axis of the fiber. Anisotropy during grating writing is one example of how PMC can be introduced within a PMF. Such an anisotropy has been observed within ordinary fiber using characterization techniques such as atomic force microscopy and side-scattered light [8–11] and its related birefringence has been calculated using different numerical methods [12, 13]. However, there are few publications focused on PMC within FBG-in-PMF. This is because the phase matching condition is not matched or even close to the Bragg period such that the efficiency of coupling over the length of the grating is poor, in contrast to long period gratings (LPGs), such as titled LPGs, spatial LPGs, and helical LPGs all written into PMF. These can operate as rocking filters [14–19]. The phase matching condition for two orthogonal polarization modes is satisfied by LPGs and not by FBGs. For PMC of FBGs, the only two examples (to our knowledge) are focused on the PMC when FBGs-in-PMF are pressed [20] and rotated [21].

White light based optical fiber coherence domain polarimetry (OCDP) [22–25] is used to test PMC here. OCDP with high sensitivity (~90 dB) and high dynamic range (~90 dB) were realized in our previous work [25]. In this paper, we focus on PMC within FBG-in-PMF which are observed by a white light based on OCDP system for the first time. Given the inefficient coupling compared to matched systems, this PMC may be too weak to be readily noticed by other methods. Weak PMC, another aspect of FBG-in-PMF, can give extra information as a complement of Bragg wavelength, which is demonstrated by a localized and long range temperature measurement. The PMC intensity of FBG-in-PMF is also discussed in

detail under the assumption of the asymmetric refractive index change in the core introduced by the FBG written process.

2. FBGs-in-PMF

2.1 Bragg reflections of FBGs-in-PMF

Two FBGs (~1.0 cm in length) are inscribed in hydrogenated Panda PMF by UV direct writing through a phase mask and UV light based side-written technology and their separation in PMF is ~3 m. The near IR transmission spectra through the FBGs-in-PMF are measured by an optical spectra analyzer (OSA), shown in Fig. 1. There are four transmission notches in the spectrum of two FBGs (Fig. 1). Each FBG produces two notches corresponding to the two polarization eigenstates of the PMF. The wavelength separation, $\Delta\lambda$, for the two FBGs is about 0.37 nm which agrees well with the specified birefringence B , $\sim 3.5 \times 10^{-4}$ - 4.0×10^{-4} .

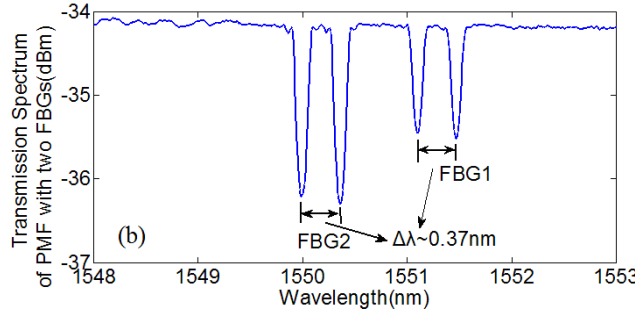


Fig. 1. The transmission spectrum of PMF with two written-in FBGs.

2.2 Observing PMCs of FBGs-in-PMF by a white light source far away from Bragg wavelengths

When the phase mask based side-written technique is used to inscribe FBGs in PMF, a non-symmetric refractive index modulation profile [8–13] can be introduced easily. When the writing FBG in PMF with an angle θ between the writing beam and one of the principal axes of the PMF, as shown in Fig. 2(a), the two polarization eigenmodes would be modulated / changed accordingly and this results the two principal axes of PMF-with-FBG rotating an angle Θ from X-Y to X'-Y', which lead to the PMC happened. The resulting axis X'-Y' caused by the non-symmetric refractive index profile could be simulated by Finite Element Method, such as the Comsol software. FBG here works like a series of rotating wave plates. The PMC could be simulated based on the coupled mode equation or the transfer matrix method without considering the reflection mode when we concern the white light far from Bragg wavelengths. Some simulation results are shown in section 4 under the assumption of an asymmetric refractive index modulation profile.

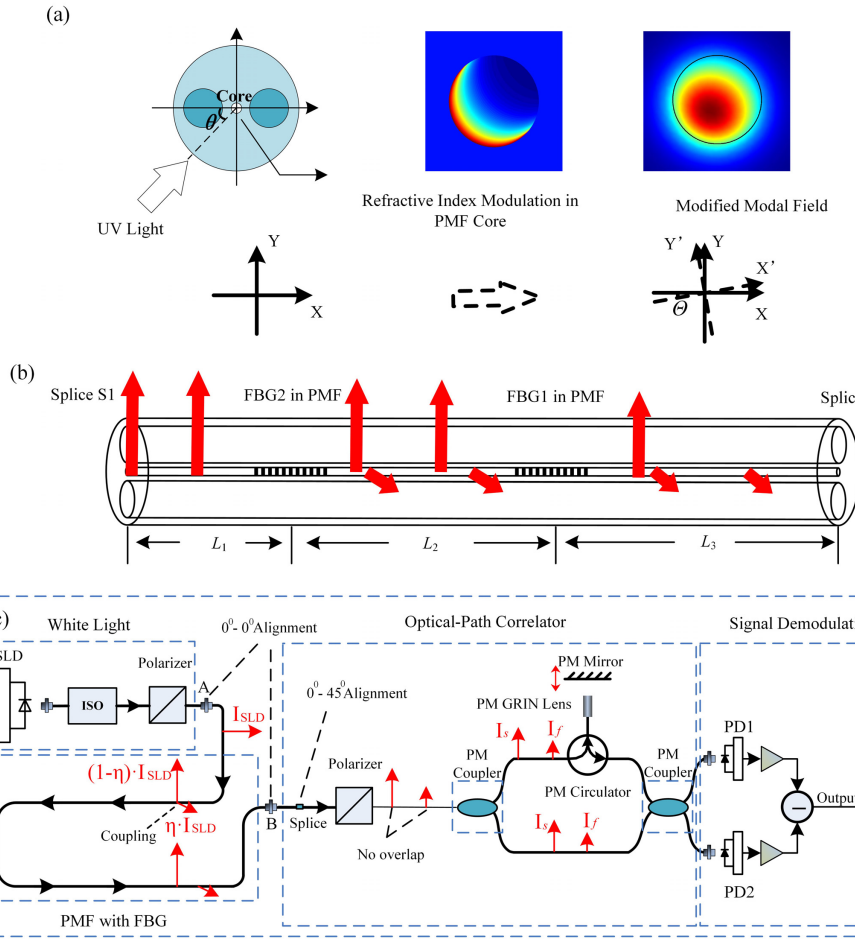


Fig. 2. (a) the asymmetric refractive index profile of FBG by side-written technology (b) the PMC of FBG-in-PMF (c) the PMC measurement based on an OCDP system.

The PMF with two FBGs, shown in Fig. 2(b), is inserted into a white light based OCDP system, as shown in Fig. 2(c). The white light source is a super luminescent diode (SLD) with the central wavelength ~ 1310 nm, bandwidth ~ 60 nm and optical output power $I \sim 2.5$ mW. Its spectrum is shown in Fig. 3(a) and the obvious OH⁻ absorption could be observed. The white light passes through an isolator and a polarizer and is coupled into the PMF. Its polarization orientation is aligned to the slow axis of the PMF. PMC between the two polarization eigenmodes can be introduced by FBGs-in-PMF, shown in Fig. 2(b). The PMC intensity is defined as $10 \cdot \log_{10}[I_{\text{coupling}}/I_0]^2$, where I_0 and I_{coupling} are the input light power and the coupling light power at the PMC position. The optical path difference between two polarization eigenmodes is decided by the product of PMF birefringence Δn and the rest PMF length, $L_2 + L_3$ when considering the PMC of the first FBG-in-PMF in Fig. 2(b). It can be measured using an optical path correlator, as shown in Fig. 2(c). Here, two 3dB polarization maintaining couplers are used to construct the MZI. The optical path difference of two arms of the MZI can be tuned by a scanning stage with a polarization maintaining mirror linked in one arm, shown as Optical-Path Correlator. The optical path scanning range could be ~ 200 mm and its insertion loss is < 1 dB. The interference signals that changed with the scanning range are detected by two photo detectors (PD) and their differential is recorded with a digital analyzer. PMC peaks could be read out from Fig. 3(b), including a few PMC peaks introduced by two splice points of PMF and two inscribed FBGs. Two stronger PMCs, S1 and S2, are introduced

by the left splice point and the right splice point of PMF in Fig. 2(b) and their PMC intensities are ~ 45 dB and ~ 47 dB. The unavoidable misalignment between the principal axes of two spliced PMF is the main reason of these PMCs. The PMC intensities of two FBGs are ~ 56 dB and ~ 59 dB. The FBGs introduced PMCs could be confirmed by comparing with the PMC measurement before inscribing FBGs and estimating the PMC position according to the birefringence of PMC. Their optical path difference is $\sim 1140 \mu\text{m}$, the separation between the coupling points is ~ 3 m according to the birefringence of $\sim 3.8 \times 10^{-4}$ at 1310 nm. The optical path difference between the splice points and FBGs all agree with the case of our PMF sample in Fig. 2(b), $L_1 = 1.5$ m, $L_2 = 3$ m and $L_3 = 5$ m. Here we observed the PMCs by using a white light source of 1310 nm, far away from Bragg wavelength of ~ 1550 nm, and its typical optical spectrum is given in Fig. 3(a). The reason is to avoid the overlap between the weak PMCs and the ripple introduced by Bragg reflections in the interference spectrum, which is explained in the next section.

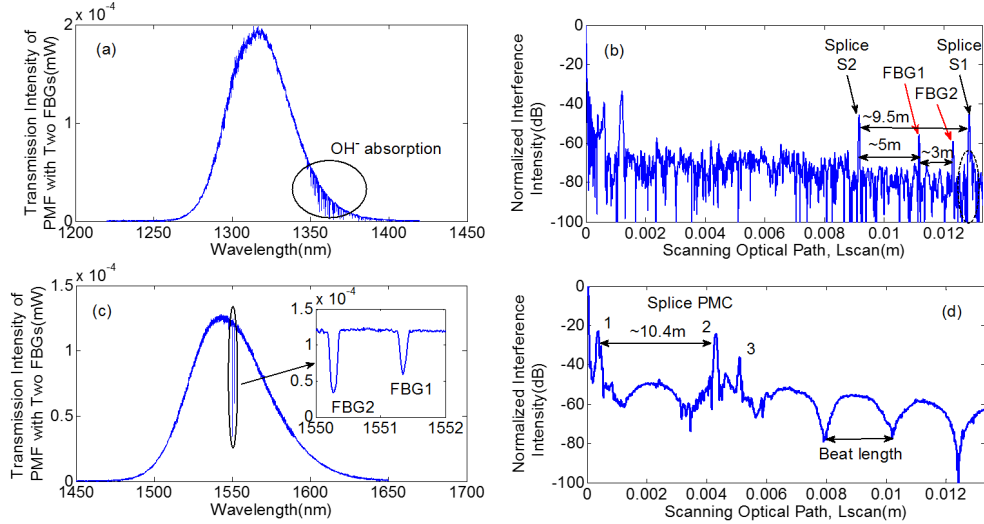


Fig. 3. (a) a SLD spectrum of 1310 nm. (b) the PMC measurement of FBGs-in-PMF based on the 1310 nm SLD: PMC peaks introduced by FBGs-in-PMF. (c) a 1550 nm SLD transmission spectrum with two written-in FBGs when the polarization orientation of SLD light is aligned to PMF slow axis. (d) the PMC measurement of FBGs-in-PMF based on the 1550 nm SLD: beat signals introduced by two FBGs-in-PMF.

2.3 Observing FBGs-in-PMF by a white light source including the Bragg wavelength

In this section, we present the results of the same PMF sample, shown in Fig. 2(b), by using the OCDP system interrogated by another white light source of 1550 nm SLD with 60nm bandwidth. The wavelengths of two FBGs-in-PMF, 1550.3 nm and 1551.3 nm, are included in the wavelength range, shown in Fig. 3(c), and their reflectivity are $R = 72\%$ and $R = 51\%$, respectively. Two FBG notches, instead of four notches in Fig. 1, establish that one polarization eigenmode is excited mainly in the PMF. The scanning interference spectrum is shown in Fig. 3(d) and the obvious beat like ripples could be found. Three PMC peaks are also found. The optical path difference between the PMC peak 1 and peak 2 introduced by PMF splice points is $\sim 3960 \mu\text{m}$, and the separation between the coupling points is ~ 10.4 m according to the birefringence of $\sim 3.8 \times 10^{-4}$, the optical path difference between the splice points agree with the PMF sample. The difference from 9.5m in Fig. 2(b) is caused by a ~ 0.9 m long PMF pigtail. Peak 3 comes from a splice point in the pigtail of 1550 nm SLD source. No PMC peak of two FBGs-in-PMF could be recognized at the corresponding position between the PMC peak 1 and peak 2. The reason is that the ripples of ~ 50 dB are stronger

than the FBG PMCs, shown in Fig. 3(b). The Beat like ripples are introduced by the Bragg reflection, which is explained in the following part.

For a simple analysis, we consider a PMF of L_{PMF_All} in length, including one PMC point and two FBGs. Here PMCs of FBGs-in-PMF are weaker compared with the background ripples, shown in Fig. 3(d). The white light, labelled as $I_{SLD}(\nu)$ in Fig. 2(c), is injected into the PMF and its polarization orientation aligned with the slow axis of the PMF. Here, the wave number, ν , is the inverse of wavelength: $\nu = 1/\lambda$. When it passes through a PMC point with a PMC coefficient, η , a small part of light will be coupled to the fast axis. Then the slow axis polarized light, labelled as $(1-\eta) \cdot I_{SLD}(\nu)$ in Fig. 2(c), and the fast axis polarized light, labelled as $\eta \cdot I_{SLD}(\nu)$ in Fig. 2(c), passes through the rest of PMF (L_{PMF_rest} in length) after which the optical path difference $\Delta n \cdot L_{PMF_rest}$ between them is accumulated. At the same time, some of the light from both eigenstates is also reflected with reflectivity $R_{FBG-i}(\nu)$ at both FBGs. The transmission signals pass through a polarizer (the principal axis is aligned 45° with the principal axis of the sensing PMF), and are converted to the same polarization state but with a different optical path $\Delta n \cdot L_{PMF_rest}$. They are coupled to two arms of MZI equally, labelled as $I_s(\nu)$ and $I_f(\nu)$ in Fig. 2(c), and can be expressed as:

$$I_s(\nu) = \frac{1}{4}(1-\eta) \cdot I_{SLD}(\nu) \cdot [1 - \sum_i R_{FBG-i}(\nu)] \quad (1)$$

and

$$I_f(\nu) = \frac{1}{4}\eta \cdot I_{SLD}(\nu) \cdot [1 - \sum_i R_{FBG-i}(\nu)] \quad (2)$$

When they pass the final PMC and reach the photo detectors (PDs), the four signals are all coupled together giving rise to a spectral interference profile described as:

$$\begin{aligned} I(\nu, L_{scan}) = & \frac{1}{2}I_s(\nu) + \frac{1}{2}I_f(\nu) + \gamma\sqrt{I_f(\nu) \cdot I_s(\nu)} \cdot \cos(2\pi\nu \cdot \Delta n \cdot L_{PMF_rest}) \\ & + \frac{1}{2}\gamma\sqrt{I_f(\nu) \cdot I_s(\nu)} \cdot \cos[2\pi\nu \cdot (\Delta n \cdot L_{PMF_rest} - L_{scan})] \\ & + \frac{1}{2}\gamma\sqrt{I_f(\nu) \cdot I_s(\nu)} \cdot \cos[2\pi\nu \cdot (\Delta n \cdot L_{PMF_rest} + L_{scan})] \\ & + \frac{1}{2}\gamma[I_f(\nu) + I_s(\nu)] \cdot \cos(2\pi\nu \cdot L_{scan}) \end{aligned} \quad (3)$$

where their total intensity, detected by the PDs, is

$$I_{total}(L_{scan}) = \int_0^{\infty} I(\nu, L_{scan}) d\nu \quad (4)$$

Here L_{scan} is the optical path difference of MZI. The degree γ of coherence of light source can be thought as a constant less than one (< 1). The first three terms in Eq. (3) are DC terms and can be removed readily. The integrals of the last three AC terms are the cosine Fourier transform (FT) between the spatial domain, L_{scan} , and the wave number domain, ν . The strongest main interference fringe of WLI is at the position of $L_{scan} = 0$, determined by the last term. $I_s(\nu) + I_f(\nu)$ includes the FBG spectra of $[1 - \sum_i R_{FBG-i}(\nu)]$ and can be reversed by the FT

of $I_{total}(L_{scan})$, which is the principle of the traditional FT spectrometer. The comparably weak two WLI fringes are generated by the second and third cosine terms in Eq. (3); the positions of the two WLI fringes are at $\Delta n \cdot L_{PMF_rest} + L_{scan} = 0$ and $\Delta n \cdot L_{PMF_rest} - L_{scan} = 0$. This provides the position information where the coupling between the two eigenmodes in the sensing PMF occurs. The ripple is a beat-like signal introduced by the difference in wavelength or wave number of the two FBGs. The integral of the last term of Eq. (3) can be simplified as

$$\begin{aligned}
& \int_0^\infty \frac{1}{2} \gamma [I_f(\nu) + I_s(\nu)] \cdot \cos(2\pi\nu \cdot L_{\text{scan}}) d\nu \\
&= \int_0^\infty \frac{1}{8} \gamma I_{\text{SLD}}(\nu) \cdot [1 - \sum_i R_{FBG-i}(\nu)] \cdot \cos(2\pi\nu \cdot L_{\text{scan}}) d\nu \\
&= \int_0^\infty \frac{1}{8} \gamma I_{\text{SLD}}(\nu) \cdot \cos(2\pi\nu \cdot L_{\text{scan}}) d\nu - \frac{1}{8} \gamma \sum_{i=1,2} I_{\text{SLD}}(\nu_i) \cdot R_{FBG-i}(\nu_i) \cdot \cos(2\pi\nu_i \cdot L_{\text{scan}}) \cdot \delta\nu_i
\end{aligned} \tag{5}$$

When considering that two FBGs reflect light at wave numbers ν_1 and ν_2 , and their bandwidths are $\delta\nu_1$ and $\delta\nu_2$. The beat signal will be introduced by last two terms in Eq. (5), including $\cos(2\pi\nu_1 \cdot L_{\text{scan}})$ and $\cos(2\pi\nu_2 \cdot L_{\text{scan}})$, when optical path difference L_{scan} of MZI is changed by scanning stage in the system. The beat length L_{beat} is decided by ν_1 and ν_2 and expressed as $L_{\text{beat}} = \frac{1}{\nu_1 - \nu_2}$. The corresponding experimental data is shown in Fig. 3(d) and

obvious beat signals are observed. Here, high frequency signals are filtered and the beat signal and the PMC signals became clear. When the wave number ν_1 or ν_2 is changed by temperature or strain applied on FBGs, the beat length shown in Fig. 3(d) would change and could be served as the signal of FBG sensors. A few PMC peaks in Fig. 3(d) are the signal introduced by fiber connectors and splice points. It needs to be mentioned that the experimental signals shown in Figs. 3(b) and 3(d) are all symmetric in $L_{\text{scan}} = 0$, which could be found in Eq. (3) as well. Only half of the symmetrical signals are shown in Figs. 3(b) and 3(d).

3. Temperature response of the PMCs and beat of two FBGs-in-PMF

We design a simple temperature experiment based on two characteristic signals, PMCs and Beat, of FBGs-in-PMF. First, we put the PMF of $L_1 + L_2$ including FBG2 on a temperature controller and the rest part of PMF including FBG1 is isolated from the temperature change. The optical path difference between PMC S1 and FBG2, shown in Fig. 2(b), is changed with temperature change and they have a linear relationship, shown in Fig. 4(a). At the same time, the beat length changed with temperature change is shown in Fig. 4(b), agreed with the

theoretical analysis, $L_{\text{beat}} = \frac{1}{\nu_1 - \nu_2}$. The theoretical results are based on the linear temperature

dependence of PMF Bragg wavelength, $\sim 10.3 \text{ pm}/^\circ\text{C}$, which is measured directly by an optical spectrum analyzer. Second, we put only $\sim 5 \text{ cm}$ long PMF (with FBG2 included in) on a temperature controller and all the other part of PMF is isolated from temperature change. The beat length introduced by FBGs gives the very-localized temperature information. The applied and measured temperature are agreed well, shown in Fig. 4(c). However, there is no obvious change of the PMC peak positions in the signal, shown in Fig. 4(c) as well. The reason is the short length of the heated PMF. The PMC peak positions don't give the very-localized information. While PMC peak positions could give the average temperature change between PMC points of PMF, proved and shown in Fig. 4(a).

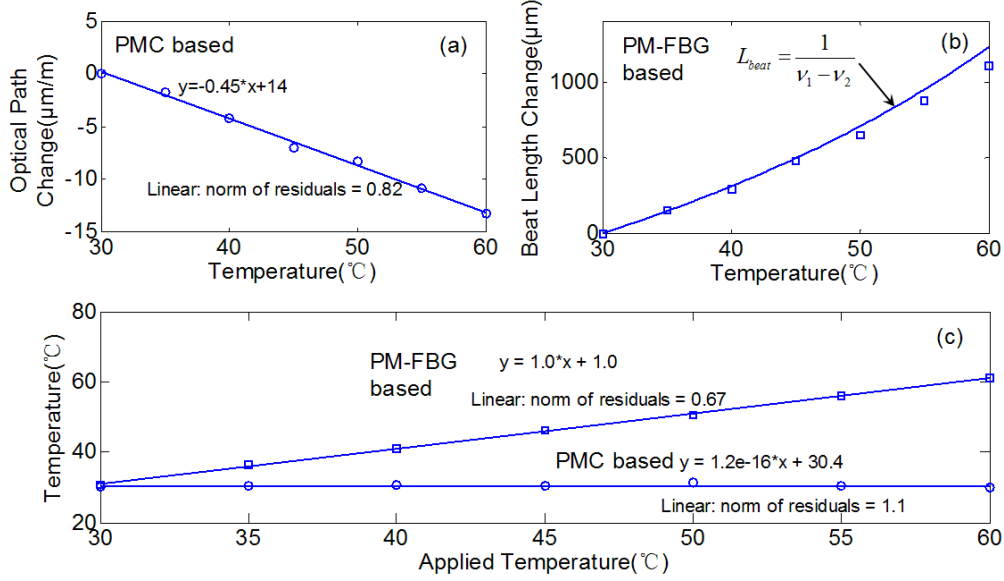


Fig. 4. (a) Temperature response of the PMC in PMF. (b) The theoretical and experimental results of the FBG beat length Vs temperature. (c) The measurement of the localized temperature change at FBG2 based on both sensing signals in (a) and (b).

It also needs to be mentioned that the beat length measurement based scheme is effective to the case of two FBGs, one as sensor the other one as a reference. Larger scanning step and less sample ratio for the scanning stage could be used to monitor the beat length in Fig. 3(d). For more than two FBG as sensors, traditional FT spectra could be used to the signal with higher frequency, and FBG spectra could be recovered and more than two FBG sensors could be demodulated. In that case, the scanning step should be reduced and the high frequency signal should be recorded in order to recover the FBG spectra, which would increase the interrogation time of the sensing system. The faster demodulation scheme may be realized by using a MZI with a piezoelectric fiber stretcher based optical path scanning strategy [26].

4. Discussions of PMCs of FBGs-in-PMF

The PMC of FBG-in-PMF may be introduced by its isotropic profile of refractive index across the PMF core, demonstrated as Fig. 2(a), which could be estimated. We assume the asymmetric refractive index profile as $\Delta n_p \cdot \exp[-2\alpha(x' + \sqrt{r^2 - y'^2})]$ as reported in [12,13],

where $\begin{cases} x' = x \cos \theta + y \sin \theta \\ y' = -x \sin \theta + y \cos \theta \end{cases}$, Δn_p is the peak refractive index change on the side where the

UV beam is incident, 2α is the asymmetry coefficient, r is the core radius. The asymmetric refractive index relates to the writing angle θ , decided by the UV radiation direction and shown in Fig. 2(a), and the polarization of the UV laser [8–13]. To estimate the PMC of FBG-in-PMF in Fig. 2(b), two polarization eigenmodes of PMF without and with refractive index modulation are simulated firstly. Secondly the coupling coefficients between two sets of eigenmodes are calculated by the normal coupled mode analysis. The FBG could be considered as a stack of rotating wave plates. So the Jones matrix could be used, similar as in [20], then the PMC of FBG-in-PMF is realized finally. It is decided by the refractive index modulation and the length of FBGs. Figure 5(a) give the periodical results of the PMC intensity changed with the FBG length for the case of $\theta = 45^\circ$ and $\Delta n_p = 5 \times 10^{-3}$. The peak refractive index modulation Δn_p is $\sim 5 \times 10^{-3}$ derived from the Bragg grating spectrum. Figure 5(b) show the results of the angle θ versus the PMC intensity. The maximum PMC could be

realized when the angle $\theta = 45^\circ$. It would be minimum at $\theta = 0^\circ$ or $\theta = 90^\circ$ where the asymmetric refractive index is modulated along two principal axes of PMF. The PMC intensity from infinitely small to ~ 45 dB could be reached at the reasonable peak refractive index change Δn_p if the condition could be controlled accurately. However, it is out of our capability at this moment.

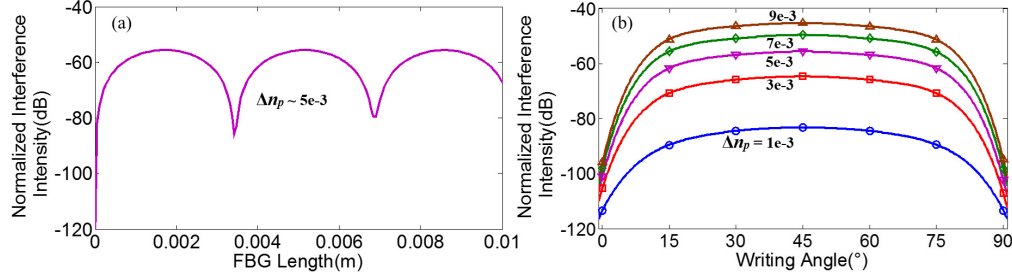


Fig. 5. (a) the simulation of the relative PMC intensities of FBGs-in-PMF Vs FBG length. (b) the simulation of the relative PMC intensities of FBG-in-PMF Vs Writing angle.

5. Conclusions

We observed and analyze the weak PMCs of two FBGs-in-PMF, -56 dB and -59 dB, by an OCDP system using a white light source of ~ 1310 nm in wavelength, far from Bragg wavelength of 1550 nm. PMCs as another complement aspect of FBGs-in-PMF besides Bragg wavelengths are demonstrated by a localized and long range temperature measurement.

Acknowledgments

Authors thank for the support by National Natural Science Foundation of China (NSFC) (No. 61377096, 61227013, and 61422505), the Program for New Century Excellent Talents in University (NCET-12-0623), Heilongjiang Young Researcher Support Project (1253G018), Harbin Science foundation (2011RFLXG004), National Key Scientific Instrument and Equipment Development Project (No. 2013YQ040815), Fundamental Research Funds of the Central University, China, and the 111 project (B13015), to the Harbin Engineering University.